Preferential accumulation of bubbles in Couette-Taylor flow patterns

Eric Climentª)
Laboratoire de Génie Chimique, UMR 5503, 5, Rue Paulin Talabot, 31106 Toulouse, France

Marie Simonnet
Arcelor Research SA, Voie Romaine, Boite Postale 30320, 57283 Maizières les Metz, France

Jacques Magnaudet
Institut de Mécanique des Fluides de Toulouse, UMR 5502, Avenue du Professeur Camille Soula, 31400 Toulouse, France

(Received 12 December 2006; accepted 30 May 2007; published online 17 August 2007)

We investigate the migration of bubbles in several flow patterns occurring within the gap between a rotating inner cylinder and a concentric fixed outer cylinder. The time-dependent evolution of the two-phase flow is predicted through three-dimensional Euler-Lagrange simulations. Lagrangian tracking of spherical bubbles is coupled with direct numerical simulation of the Navier-Stokes equations. We assume that bubbles do not influence the background flow (one-way coupling simulations). The force balance on each bubble takes into account buoyancy, added-mass, viscous drag, and shear-induced lift forces. For increasing velocities of the rotating inner cylinder, the flow in the fluid gap evolves from the purely azimuthal steady Couette flow to Taylor toroidal vortices and eventually a wavy vortex flow. The migration of bubbles is highly dependent on the balance between buoyancy and centripetal forces (mostly due to the centripetal pressure gradient) directed toward the inner cylinder and the vortex cores. Depending on the rotation rate of the inner cylinder, bubbles tend to accumulate alternatively along the inner wall, inside the core of Taylor vortices or at particular locations within the wavy vortices. A stability analysis of the fixed points associated with bubble trajectories provides a clear understanding of their migration and preferential accumulation. The location of the accumulation points is parameterized by two dimensionless parameters expressing the balance of buoyancy, centripetal attraction toward the inner rotating cylinder, and entrapment in Taylor vortices. A complete phase diagram summarizing the various regimes of bubble migration is built. Several experimental conditions considered by Djéridi, Gabillet, and Billard [Phys. Fluids **16**, 128 (2004)] are reproduced; the numerical results reveal a very good agreement with the experiments. When the rotation rate is increased further, the numerical results indicate the formation of oscillating bubble strings, as observed experimentally by Djéridi *et al.* [Exp. Fluids **26**, 233 (1999)]. After a transient state, bubbles collect at the crests or troughs of the wavy vortices. An analysis of the flow characteristics clearly indicates that bubbles accumulate in the low-pressure regions of the flow field. © *2007 American Institute of Physics*. [DOI: 10.1063/1.2752839]

I. INTRODUCTION

Understanding and predicting the behavior of bubbles in complex flow patterns is of major interest for many practical applications. Industrial facilities are often designed to achieve separation or mixing of two-phase fluid flows. Chemical engineering, the oil industry, and transformation of thermal energy are all areas in which two-phase flow modeling is of great concern. Centrifugal separators are widely employed in manufacturing processes. Hydrocyclones are commonly used to separate the phases in bubbly flows. Migration of a dispersed phase (bubbles, drops, or particles) is basically controlled by the spatial structure of the carrying fluid flow. It is important to achieve the prediction of preferential accumulation of bubbles, as it may dramatically modify transfer phenomena occurring in the two-phase mixture. More generally, the presence of bubbles dispersed in a turbulent flow modifies the dynamics of vortical structures through mutual interactions. For instance, when bubbles are collecting along a heated wall, thermal convection is significantly enhanced by fluid agitation. In contrast, if the bubbles are attached to the wall, the global heat exchange coefficient is significantly reduced.

In the present paper, we focus on a simple geometry, namely the flow between two vertical concentric cylinders. The gap between the cylinders is filled with a Newtonian fluid seeded with small bubbles. Bubbles migrate under the influence of gravity and hydrodynamic forces responding to different flow characteristics. This simple geometry has several advantages. It provides an adequate configuration to precisely compare numerical simulations with experiments.[1,2] When the inner cylinder rotation gradually increases, the fluid flow within the gap undergoes successive bifurcations, which finally lead to turbulence. This sequential transition to fully developed turbulence emphasizes the role of coherent structures in bubble dispersion. Even in a fully turbulent

ª)Author to whom correspondence should be addressed. Electronic mail: Eric.Climent@ensiacet.fr

flow, well-defined vortices that appear in early stages of Couette-Taylor flows persist. Indeed, for high rotation rates of the inner cylinder, migration of bubbles is still related to large-scale flow patterns.[3] This academic geometry is also close to practical applications such as centrifugal separators (cyclones) or mixing devices. Chaotic mixing of inertial particles has been investigated with simplified models of the flow[4,5] in such configurations.

When the inner cylinder rotates, the selection of the flow pattern is controlled by a centrifugal instability of the purely azimuthal Couette flow, and toroidal steady vortices (Taylor vortex flow) occur beyond a first threshold. While the Taylor number (see Sec. II for definition) increases above the threshold of the second instability, the flow becomes time-dependent as vortices undergo wavy oscillations (wavy vortex flow). Increasing further the Taylor number (related to the nondimensional centrifugal forcing) induces a modulation of the wavy shape of the vortices; eventually turbulence sets in gradually. Bubbles injected in these various flow patterns have intricate responses. Early observations by Shiomi *et al.*[6] showed that bubble accumulation forms geometrical arrangements like rings and spirals. In these experiments, the axial volumetric fluxes of air and water were varied for different rotation rates of the inner cylinder. The authors were able to summarize the numerous two-phase flow patterns in a configuration map, but the underlying physics remained unclear. Later, Atkhen *et al.*[3] studied a highly turbulent Couette-Taylor flow with axial fluid flux. The flow was seeded with small air bubbles to make visualization of spiral vortices easy. The authors observed that bubbles collect at particular locations along the inner wall. More precisely, bubbles were attracted in outflow regions where the fluid flows radially from the inner cylinder toward the outer wall. Those locations correspond to low-pressure areas. The authors used bubbles as tracers of the traveling Taylor vortices. A precise understanding of the mutual interactions between the continuous fluid phase and the dispersed bubbles started with the experimental study of Djeridi *et al.*[2] These authors carried out a series of experiments based on the observation of bubble migration within Taylor vortices. A more comprehensive inspection of arrangements of the dispersed phase together with flow structure modulations induced by bubbles was also presented by Djeridi *et al.*[1] Bubbles were condensable (generated by cavitation) or noncondensable (originating from free surface agitation). Results were compared to simplified models providing a prediction of the average distance between consecutive rings of bubbles. Modifications of the flow structure and instability thresholds were also reported.

In the present study, we investigate numerically the migration of spherical bubbles in three different regimes of the flow between two concentric cylinders [namely Couette flow, Taylor vortex flow (TVF), and wavy vortex flow (WVF)]. Using Lagrangian tracking of bubbles coupled with a direct numerical simulation of the full Navier-Stokes equations allows us to address the following open issues. What are the respective roles of the forces experienced by the bubbles during their entrapment in Taylor vortices? What are the dimensionless parameters determining the number of bubble rings over one wavelength of the TVF? Where are the accumulation regions in the WVF regime?

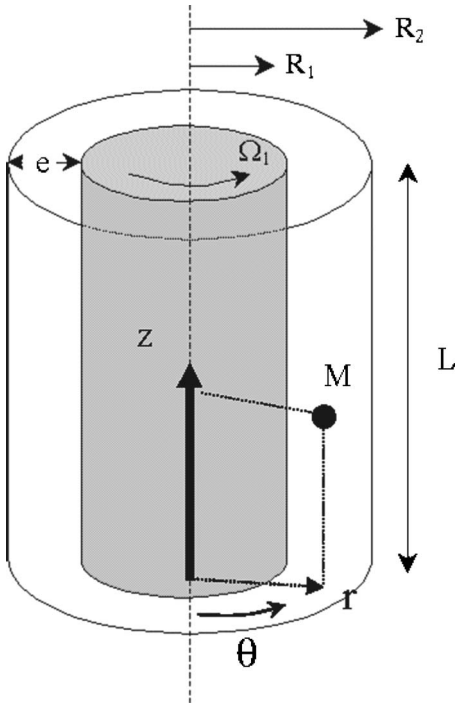

FIG. 1. Sketch of the geometrical configuration used in the computations ($e=R_2-R_1$: gap width; $\eta=R_1/R_2=0.889$; $L=2e$; periodic boundary conditions are applied in the axial direction).

Since there has been significant progress over the past two decades in obtaining knowledge on the forces acting on bubbles,[21] Lagrangian tracking has become a relevant tool to investigate bubble dispersion in complex flows. Analytical expressions of the forces with extended validity are now available and provide a sound background for predicting preferential accumulation. The major role played by coherent structures in a fully turbulent flow was emphasized by Sene *et al.*[7] and Poorte and Biesheuvel.[8] Understanding the accumulation process is a key step toward predicting bubble-induced modifications of the carrying fluid flow. Indeed, a small amount of dispersed phase located in the core of vortices can induce dramatic changes in the vortex structure.[9,10]

This paper is organized as follows. The next section is devoted to the description of the governing equations of the two-phase flow (some details on the numerical methods and validation of the flow are also included). The third section gathers results on bubble dispersion in Couette-Taylor flows in the first three flow regimes previously discussed. Frequent comparisons with the experimental observations of Djéridi *et al.*[1,2] are provided. The concluding section includes a comprehensive scenario of the entrapment phenomena.

II. TWO-PHASE FLOW SIMULATIONS

A. Direct numerical simulations of the carrying flow

The fluid between the two vertical cylinders (see Fig. 1 for a sketch of the configuration) is considered Newtonian and incompressible with constant physical properties (ρ_f is

the fluid density and μ is the dynamic viscosity). The unsteady three-dimensional Navier-Stokes equations governing the flow read

$$\nabla \cdot \mathbf{u} = 0, \tag{1a}$$

$$\rho_f \left(\frac{\partial \mathbf{u}}{\partial t} + \mathbf{u} \cdot \nabla \mathbf{u} \right) = -\nabla \mathrm{P} + \nabla \cdot [\mu(\nabla \mathbf{u} + \nabla^{\mathrm{T}} \mathbf{u})]. \tag{1b}$$

These equations are directly solved using a conservative finite-volume method. Primitive variables (the velocity $\mathbf{u}$ and pressure P) are discretized on a staggered nonuniform grid. Spatial derivatives are computed with second-order accuracy. Temporal integration is achieved through a third-order Runge-Kutta scheme and a semi-implicit Crank-Nicolson scheme for the viscous terms. The corresponding code has been widely used and validated in laminar and turbulent flow regimes (see, e.g., Refs. 11 and 12 and references therein). The fluid is confined between two concentric vertical cylinders (with radii R_1 and R_2). The radii ratio $\eta = R_1/R_2$ characterizes the geometry and is set to 8/9. Cylinders of infinite axial extension are modeled using periodic boundary conditions in the axial direction. We assume that the flow distortion produced by the actual boundary conditions at both ends of the experimental device (i.e., top and bottom walls of the cylinders) has a negligible influence on bubble dispersion far from these walls. Using periodic boundary conditions for the direct numerical simulation of confined cellular flows has proven to be an efficient and reliable model (see, for instance, Ref. 13 in the context of Couette-Taylor flows). The height of the numerical domain is $L = 2(R_2 - R_1)$, i.e., twice the gap. It allows the simulation of one wavelength of the Taylor vortex flow. Grid cells are uniform in the axial and azimuthal directions. We use stretched grids in the radial direction to better describe the vicinity of the cylinder walls. Two-dimensional simulations are performed using 60×60 grid cells in the $\mathbf{e}_r - \mathbf{e}_z$ directions, while the azimuthal direction ($\mathbf{e}_\theta$) is discretized using 32 or 64 uniform cells, depending on the wavelength of the azimuthal oscillations in the wavy vortex regime. The outer cylinder is kept fixed while the inner cylinder rotates with a constant angular rotation rate Ω. In what follows, all quantities related to the flow will be scaled using the gap $e = R_2 - R_1$ and the reference velocity ΩR_1. We define the Taylor number as $\mathrm{Ta} = \Omega^2 R_1 (R_2 - R_1)^3 / \nu^2$, where $\nu = \mu/\rho_f$ is the kinematic viscosity of the fluid. The behavior of the flow can be characterized either by the Taylor number or by the Reynolds number $\mathrm{Re} = \Omega R_1 (R_2 - R_1)/\nu$.

For $\mathrm{Ta} < \mathrm{Ta}_o$ (Ta_o being the critical Taylor number corresponding to the first instability), the flow is purely azimuthal, so we have

$$u_\theta(r) = Ar + \frac{B}{r} \quad \text{with } A = -\frac{\Omega_1}{(R_2/R_1)^2 - 1} \quad \text{and}$$

$$B = \frac{\Omega_1 R_2^2}{(R_2/R_1)^2 - 1}, \quad u_r = u_z = 0. \tag{2}$$

The corresponding torque G_0 experienced by the inner cylinder is then

$$G_0 = \frac{4\pi\mu R_1^2 \Omega_1}{1 - (R_1/R_2)^2}. \tag{3}$$

We checked that both the velocity field and the torque exerted on the cylinder are predicted within 10^{-6} relative error in our numerical simulations.

The next regime (TVF) occurs when Ta exceeds the critical value Ta_o. In this case, the fluid flow forms counter-rotating cells in the $(\mathbf{e}_r - \mathbf{e}_z)$ plane that are invariant in the azimuthal direction (toroidal vortices, see Fig. 2).

To check the stability of the Couette flow with increasing rotation rate, we introduced a weak perturbation and examined its growth rate σ. We evaluated the critical Taylor number Ta_o to 1958, which corresponds to a critical Reynolds number $\mathrm{Re}_o = 125$. The evolution of σ as a function of the reduced Taylor number $\varepsilon_{\mathrm{Ta}} = (\mathrm{Ta} - \mathrm{Ta}_o)/\mathrm{Ta}_o$ or the reduced Reynolds number $\varepsilon_{\mathrm{Re}} = (\mathrm{Re} - \mathrm{Re}_o)/\mathrm{Re}_o$ is nearly linear and allows a precise determination of Ta_o. The estimate of Ta_o provided by the direct numerical simulation is in very good agreement with available theoretical studies: Chandrasekhar[14] found $\mathrm{Ta}_o = 1801$ while Di Prima and Swinney[15] obtained $\mathrm{Ta}_o = 1956$ from linear stability analysis. As the Reynolds number is further increased beyond the threshold, the intensity of the toroidal vortices gradually grows up. In Fig. 3, the maximum velocity of the Taylor vortices is plotted for increasing ε. The evolution follows a square root law characteristic of a supercritical bifurcation.

When the angular velocity of the inner cylinder is increased further, a new bifurcation occurs at a second critical Taylor number Ta_1.[16] Toroidal cells oscillate in the azimuthal direction as a wavy modulation propagates. This flow state is known as the wavy vortex flow (WVF). Again, to track the transition from the TVF to the WVF regime, we added a weak perturbation with an imposed azimuthal wave number k_θ to the TVF. By recording the value of the growth rate σ, we obtained the value of the second critical Taylor number as $\mathrm{Ta}_1 = 2689$, which corresponds to $\mathrm{Re}_1 = 147$. These values are in good agreement with those reported in the literature. For instance, Coles[17] proposed an empirical relation between Ta_o and Ta_1, namely

$$1.86 \left[\frac{R_1}{e} \left(1 - \frac{\mathrm{Ta}_o}{\mathrm{Ta}_1} \right) \right]^{1/2} = 2.9. \tag{4}$$

Given the value we found for Ta_o, (4) indicates $\mathrm{Ta}_1 = 2813$, which is in the range of our simulations. Fenstermacher *et al.*[18] investigated experimentally a Couette-Taylor system and obtained $\mathrm{Re}_1/\mathrm{Re}_o = 1.2$, which is close to our numerical result 1.17. Finally, we plotted the evolution of the torque versus ε and compared it with some theoretical predictions and experimental results. From Fig. 4, we conclude that our simulations are able to reproduce accurately the basic features of Couette-Taylor flow patterns, both in two-dimensional and in fully three-dimensional regimes.

B. Lagrangian tracking of bubbles

The dispersed phase is made of small bubbles (the typical bubble diameter is 100 μm) experiencing the combined effects of the carrying fluid flow and the buoyancy force.

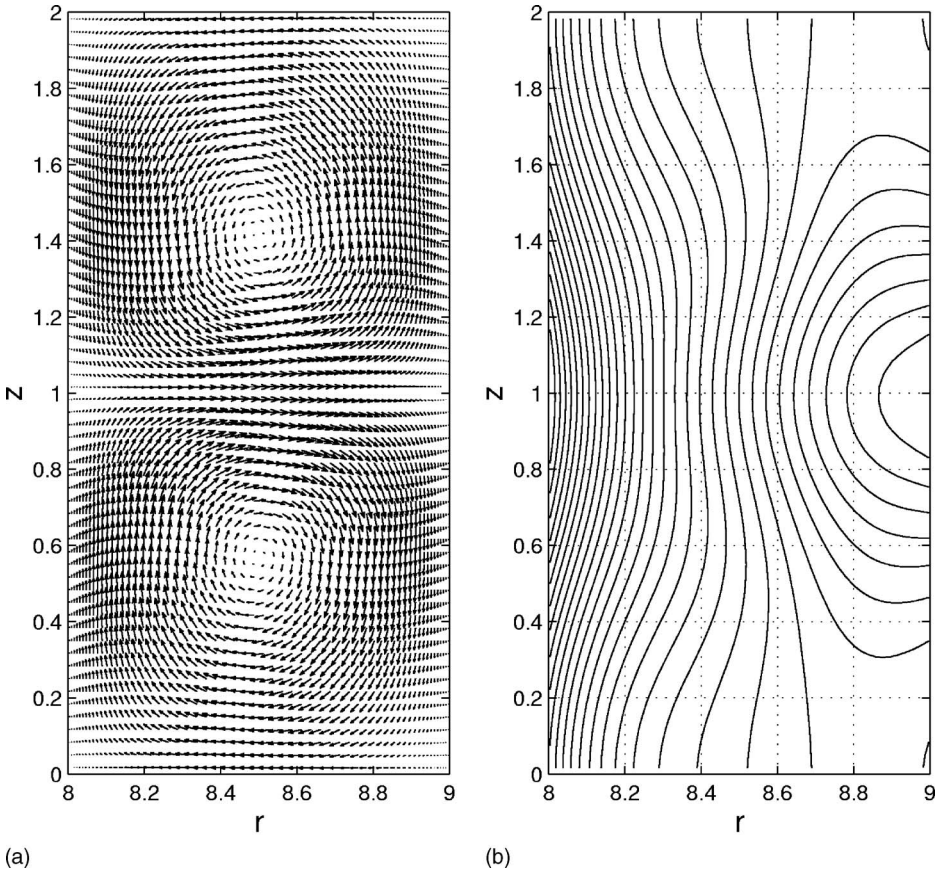

FIG. 2. Toroidal flow pattern in the Taylor vortex flow regime. *a*, velocity field; *b*, pressure contours (low pressure on the inner wall, $r=8$).

Bubble trajectories are distinct from fluid element paths and an accurate balance of the forces acting on the bubbles is required to achieve a relevant prediction of the dispersion. Obtaining an analytical expression for all hydrodynamic forces is still an open issue in most flow regimes. Therefore, simplifying assumptions have to be adopted to make the problem tractable and obtain a reasonable force balance. In experiments,[1,2] the bubbles are typically 50 times smaller than the gap width. Therefore, we aim at simulating the dispersion of small bubbles when the flow is only composed of large-scale patterns, as is the case in the first three regimes encountered by increasing the Taylor number from rest. Considering that all the relevant spatial length scales of the carrying flow are much larger than the typical size of the bubbles, we assume that the so-called Fàxen corrections[19,20] induced by the local curvature of the flow velocity field are negligible in the expression of all hydrodynamic forces. Also, in the range of bubble diameters considered in the

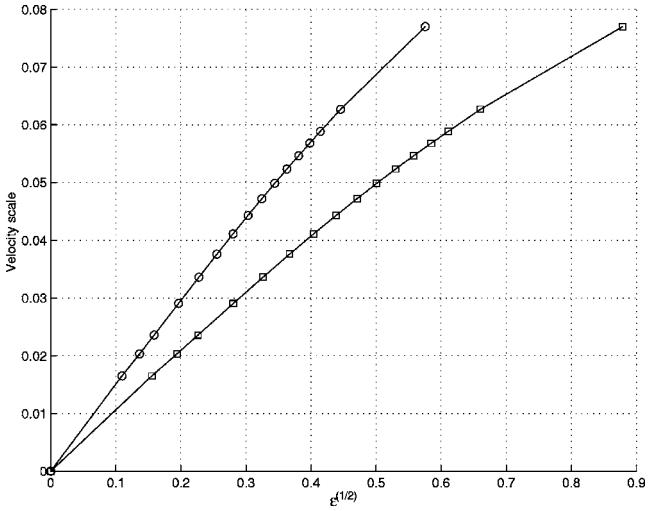

FIG. 3. Velocity scale of the secondary flow vs the distance to the threshold [$\varepsilon_{\mathrm{Re}}=(\mathrm{Re}-\mathrm{Re}_o)/\mathrm{Re}_o$: squares; $\varepsilon_{\mathrm{Ta}}=(\mathrm{Ta}-\mathrm{Ta}_o)/\mathrm{Ta}_o$: circles].

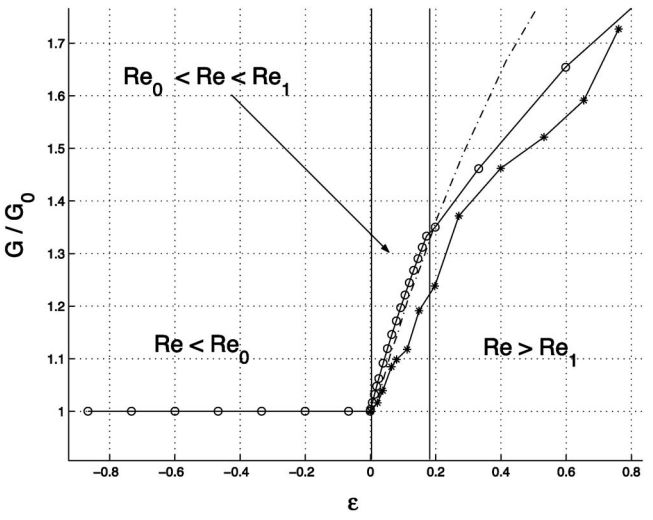

FIG. 4. Evolution of the torque on the inner cylinder with $\varepsilon_{\mathrm{Re}}$ ($\varepsilon_{\mathrm{Re}}=0$ transition to TVF; $\varepsilon_{\mathrm{Re}}=0.176$ transition to WVF). *: Experiment from Donnelly and Simon (Ref. 35); – – –·: theoretical prediction [Davey (Ref. 36)]; ○: present computations.

present paper, the effects of surface tension are strong enough to keep the bubbles spherical. Indeed, small bubbles (with diameter ranging from 100 μm to 1 mm) rising in water or glycerol/water solutions have a Reynolds number based on the slip velocity that varies from O(1) to O(10^2), whereas their Weber number (characterizing the relative strength of inertia and surface tension) is in the range O(10^{-3})–O(10^{-1}). Therefore, their deformation is negligibly small, making it reasonable to consider them spherical. Finally, we assume that the bubble surface is free of surfactant, so that the liquid slips along the liquid-air interface. In addition to the above assumptions, we assume that direct interactions between bubbles are negligible, which restricts our investigation to configurations with low bubble volume fractions. We write the force balance on each bubble as a sum of distinct contributions. Hence, we track the bubble trajectories and predict the position $\mathbf{x}(t)$ of their center of mass and their velocity $\mathbf{v}(t)$ in a fluid flow whose velocity, Lagrangian acceleration, and vorticity at $\mathbf{x}(t)$ are $\mathbf{u}$, $D\mathbf{u}/Dt$, and $\boldsymbol{\omega}=\nabla\times\mathbf{u}$, respectively, by solving

$$\frac{d\mathbf{x}}{dt}=\mathbf{v},\quad \rho_p \mathrm{V}\frac{d\mathbf{v}}{dt}=\mathbf{F} \tag{5}$$

with

$$\mathbf{F}=(\rho_p-\rho_f)\mathrm{V}\mathbf{g}+\rho_f \mathrm{V}\frac{D\mathbf{u}}{Dt}-\rho_f\frac{3V}{8R}C_D|\mathbf{v}-\mathbf{u}|(\mathbf{v}-\mathbf{u})$$
$$+\rho_f VC_M\left(\frac{D\mathbf{u}}{Dt}-\frac{d\mathbf{v}}{dt}\right)-\rho_f VC_L(\mathbf{v}-\mathbf{u})\times\boldsymbol{\omega}, \tag{6}$$

where ρ_p (ρ_f) denotes the bubble (liquid) density, V (R) is the bubble volume (radius), and C_D, C_M, and C_L are the drag, added mass, and lift coefficients, respectively. The various forces taken into account in Eq. (6) are the buoyancy force, the so-called pressure gradient force due to the Lagrangian acceleration of fluid elements, the drag force, the added-mass force, and the shear-induced lift force. Owing to the shear-free boundary condition experienced by the bubble surface, the history force is negligible for moderate bubble accelerations, as was shown in Refs. 21 and 22. For spherical bubbles, the added-mass coefficient C_M is known to be constant and equal to $\frac{1}{2}$ whatever the Reynolds number.[21–23] The drag coefficient C_D depends on the instantaneous bubble Reynolds number $\mathrm{Re}_p=2|\mathbf{v}-\mathbf{u}|R/\nu$. As we are mostly concerned with bubble Reynolds numbers in the range 0.1–10, we select a C_D correlation based on results obtained in direct numerical simulations with $\mathrm{Re}_p<50$, namely[23]

$$C_D(\mathrm{Re}_p)=16(1+0.15\mathrm{Re}_p^{1/2})/\mathrm{Re}_p. \tag{7}$$

For high-Re_p bubbles (say $\mathrm{Re}_p>50$), the mechanisms that control lift effects are essentially of inviscid nature, so that the inviscid result $C_L=\frac{1}{2}$ is appropriate.[24] At lower Re_p, it was shown[24] that C_L is a function of both the Reynolds number and the shear rate, but both dependencies are weak down to $\mathrm{Re}_p=10$. In contrast, for bubble Reynolds numbers typically less than unity, the situation becomes much more complex. Velocity gradients in the base flow contribute to induce $O(\mathrm{Re}_P^{1/2})$ lift forces through a combined effect of viscosity and inertia, so that the inertial scaling becomes irrelevant. Moreover, in contrast to the high-Reynolds-number situation, strain and rotation combine in a nonlinear way in the generation of lift effects. This is why no general expression of the lift force applicable to an arbitrary linear flow field is available to date in this regime, even though some attempts have been made toward this direction.[26] Note that these complex physics may even in certain cases reverse the sign of the lift force as compared to the inviscid prediction.[25,27]

As we expect our bubbles to have Reynolds numbers down to $O(10^{-1})$, the above discussion suggests that the expression of the lift force to be selected has to be carefully justified. For this purpose, we examined the eigenvalues of the velocity gradient tensor $\mathbf{D}=\nabla\mathbf{u}$ in the Taylor vortex flow configuration (Fig. 2), which is the main focus of our study. Four distinct regions emerged from this analysis. Not surprisingly, the core of the vortices ($r/e=8.5$, $z/e=0.5$, and $z/e=1.5$ in Fig. 2) corresponds to a solid body rotation flow. In the outflow region ($r/e=8$ and $z/e=1$), the flow is dominated by strain effects. However, it will be shown in the next section that bubble migration is mostly controlled by the phenomena taking place in the other two regions of the flow corresponding to negative vertical motion of the fluid aside from the vortex cores ($r/e=8.25$ and $z/e=1.5$; $r/e=8.75$ and $z/e=0.5$). The analysis of the eigenvalues of $\mathbf{D}$ revealed that the velocity field is close to a pure linear shear flow in these regions. Consequently, as a first attempt, we may consider that the lift force acting on the bubbles is dominated by shear effects at least during the stages where this force plays a crucial role in the lateral migration process. For this reason, we found it reasonable to focus on results available for the lift force in pure shear flows and selected the empirical expression of the shear-induced lift coefficient C_L proposed by Magnaudet and Legendre,[26] namely

$$C_L=\left[\left(\frac{6}{\pi^2}\frac{2.2555}{\left(1+0.2\left(|\mathbf{v}-\mathbf{u}|^2/G\nu\right)\right)^{3/2}}\left(\frac{\nu}{GR^2}\right)^{1/2}\right)^2+\left(\frac{1}{2}\frac{1+\left(16/\mathrm{Re}_P\right)}{1+\left(29/\mathrm{Re}_p\right)}\right)^2\right]^{1/2}, \tag{8}$$

where G stands for the local shear rate. Expression (8) matches the two asymptotic behaviors of C_L in a simple shear. The first term on the right-hand side is the low-Re_P expression of C_L while the second term fits the moderate-to-high Re_P behavior and tends toward the asymptotic value $C_L=\frac{1}{2}$ at large Re_P. Therefore, at low-to-moderate Reynolds number, the lift coefficient (8) combines the effects corresponding to both the low-but-finite-Re_P Saffman mechanism and the inertial Lighthill-Auton mechanism. Expression (8) depends on both the relative Reynolds number Re_P and the shear intensity G through Saffman's length scale $(\nu/G)^{1/2}$. Figure 5 displays the C_L values provided by expression (8) in the TVF regime with bubble characteristics corresponding to the experiments of Djeridi *et al.*[1] ($\mathrm{Re}_p=0.9$). The gray scale corresponds to values of C_L ranging from 0.37 (white) to 2.5 (black). In the TVF regime, most bubbles are likely to stay in the vicinity of regions where C_L is in the range 1.0–1.8. Based on the analysis of the eigenvalues of the velocity gra-

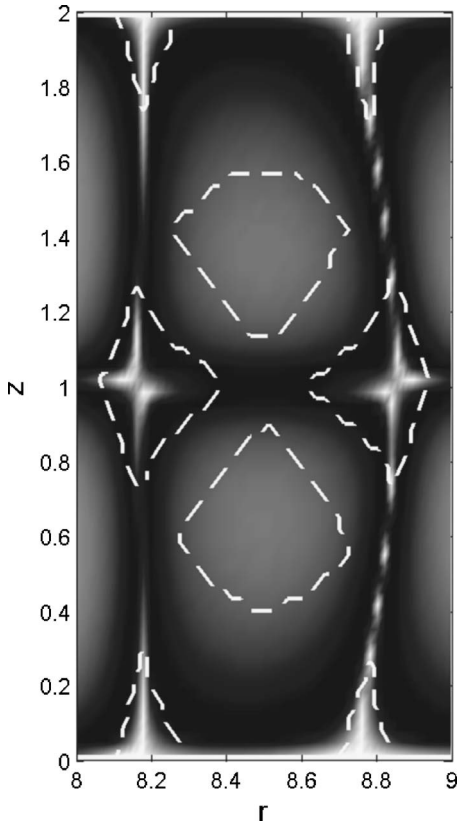

FIG. 5. Map of the lift coefficient (1 mm diameter bubbles with $V_L=2.72\times10^{-2}$ m/s in a glycerol/water solution with $\nu=3.0\times10^{-5}$ m^2/s). C_L varies from 0.37 (white) to 2.5 (dark). The dashed line corresponds to $\|\lambda_i|-|\lambda_r\|/\max(\|\lambda_i|-|\lambda_r\|)=0.3$.

dient tensor, the dashed line gives an idea of the regions where the flow is close to a pure shear flow [strictly speaking, the dashed line corresponds to $\|\lambda_i|-|\lambda_r\|/\max(\|\lambda_i|-|\lambda_r\|)=0.3$, where λ_r and λ_i stand for the real and imaginary parts of the eigenvalues of $\mathbf{D}$, respectively]. In these regions, the shear strength $2GR/|\mathbf{v}-\mathbf{u}|$ may be large, leading to high values of C_L for such low Re_p. Within the closed regions bounded by the dashed line, the flow is close to a solid-body rotation ($r=8.5$; $z=0.6$ or 1.4) or to a pure straining motion ($z=1$; $r=8.2$ or 8.8).

Expression (8) will be used in all simulations concerned with the TVF regime. When the flow depends on the azimuthal direction (WVF) we simply impose a constant lift coefficient $C_L=0.5$, as situations in which the flow exhibits multiple directions of inhomogeneity are still too complex to obtain either a theoretical or a numerical estimate of the variations of the lift coefficient with Re_P and $(GR^2/\nu)^{1/2}$. Nevertheless, based on a test performed in the TVF regime (see below), we do not expect this simplification to have a significant impact on the position of the stable fixed points.

All terms in (6) are evaluated using the characteristics of the instantaneous flow field at the exact position $\mathbf{x}$ of the bubble. Since the bubble location generally differs from the location of the mesh grid points used in the flow simulation, an interpolation procedure is required. A second-order interpolation scheme is employed to ensure accuracy and stability of the trajectory computation. The set of ordinary differential equations (6) is solved using a fourth-order Runge-Kutta scheme. The trajectory equations are integrated in a cylindrical system of axes whose unit vectors are $(\mathbf{e}_r,\mathbf{e}_\theta,\mathbf{e}_z)$ in the radial, azimuthal, and axial direction, respectively. Inertial terms due to the rotating axes system arise in the force balance, as $d\mathbf{v}/dt$ and $D\mathbf{u}/Dt$ involve centrifugal contributions. Therefore, in the particular case of TVF (in which the velocity field is independent of the azimuthal angle θ), Eq. (6) becomes

$$C_M\left(\frac{d_2\mathbf{v}}{dt}-\frac{v_\theta^2}{r}\mathbf{e}_r\right)=-\mathbf{g}+(1+C_M)\left(\frac{\partial\mathbf{u}}{\partial t}+(\mathbf{u}\cdot\nabla)_2\mathbf{u}-\frac{u_\theta^2}{r}\mathbf{e}_r\right)-\frac{3}{8R}C_D|\mathbf{v}-\mathbf{u}|(\mathbf{v}-\mathbf{u})-C_L(\mathbf{v}-\mathbf{u})\times\boldsymbol{\omega}, \tag{9}$$

where the bubble density has been neglected. In Eq. (9), which is only solved in the r and z directions, $d_2\mathbf{v}/dt$ $[(\mathbf{u}\cdot\nabla)_2\mathbf{u}]$ stands for the acceleration of the bubble (the advective acceleration of the fluid) calculated in a fixed $(\mathbf{e}_r,\mathbf{e}_z)$ plane. For the TVF regime, we assume that v_θ and u_θ are equal, which means that bubbles are perfectly entrained by the fluid in the azimuthal direction. This is reasonable because in this direction there is no component of the buoyancy force, nor of the fluid acceleration, which could induce a significant slip velocity. In the WVF regime, we checked that the nonzero azimuthal component of the fluid acceleration remains weak compared to the other two components. However, in this fully three-dimensional regime, all three components of Eqs. (1) and (6) are solved without any extra simplifying assumption. Using $C_M=1/2$ and defining $V_L=2\tau g$ as the mean slip velocity of the bubbles along the vertical axis $\mathbf{e}_z$, we may write Eq. (9) in a simplified form suitable for numerical integration in the TVF regime, namely

$$\frac{d_2\mathbf{v}}{dt}=\frac{V_L}{\tau}\mathbf{e}_z+\frac{\mathbf{u}-\mathbf{v}}{\tau}+3\left(\frac{\partial\mathbf{u}}{\partial t}+(\mathbf{u}\cdot\nabla)_2\mathbf{u}\right)-2\frac{u_\theta^2}{r}\mathbf{e}_r-2C_L(\mathbf{v}-\mathbf{u})\times\boldsymbol{\omega}. \tag{10}$$

The nonlinear evolution of the drag force with Re_p is included in the definition of the bubble relaxation time τ. The net centripetal term $-u_\theta^2/r$ is due to the radial pressure gradient induced by the fluid rotation.

III. BUBBLE DISPERSION AND ACCUMULATION

Bubble transport in vortical flows exhibits some generic features. Local pressure gradient, added mass, and lift forces induce an accumulation of small bubbles in low-pressure regions of the flow. Such low-pressure zones frequently correspond to vortex cores. However, in rotating systems they may also correspond to regions close to the rotation axis. As the bubble diameter increases for fixed flow conditions, buoyancy effects become dominant and the rising speed increases, eventually leading to a uniform dispersion of bubbles throughout the flow. The first two hydrodynamic regimes of the Couette-Taylor flow provide a convenient background to explore these possibilities in detail.

In the present case, the flow is purely azimuthal at low Taylor number. Therefore, bubbles initially seeded at random positions are attracted by the rotating inner wall, which corresponds to the low-pressure region of the flow. Their lateral migration toward the inner wall is driven by the added-mass and pressure gradient contributions $-u_\theta^2/r\mathbf{e}_r$. After multiple bounces on the wall, bubbles stay in the vicinity of the inner cylinder (we use a purely elastic model of bouncing in which the normal velocity of the bubble is reversed when the distance from the bubble center to the wall becomes smaller than the bubble radius). Along the vertical direction, the vertical balance between the buoyancy and drag forces results in a constant slip velocity of the bubbles. Hence, they uniformly accumulate along the inner cylinder as long as the Couette flow is stable.

A. Accumulation of bubbles in the Taylor vortex flow regime

While the rotation rate gradually increases, the flow bifurcates toward the Taylor vortex flow regime. The force balance over each bubble is then dominated by three main contributions. Similar to what we noticed in the Couette flow regime, the centripetal force directed toward the inner wall makes the bubbles move radially while buoyancy makes them move vertically. The picture changes dramatically in the TVF regime, owing to the cellular structure of the secondary flow. The vertical balance between buoyancy and drag results in an upward slip velocity which, for sufficiently small bubbles, is smaller than the maximum downward velocity of the fluid. If inertia effects were absent, the combination of this slip velocity and of the secondary flow velocity would result in closed bubble trajectories within each toroidal eddy (see Marsh and Maxey[28] for an example with solid particles in cellular flows). The addition of inertial effects (pressure gradient, added mass, and lift forces) in the trajectory equation breaks this periodicity and force the bubbles to spiral toward particular locations in the flow. The entrapment positions correspond to stable fixed points where the force balance in the $(\mathbf{e}_r-\mathbf{e}_z)$ plane is satisfied with zero bubble acceleration and velocity, namely

$$\mathbf{0} = \frac{V_L}{\tau}\mathbf{e}_z + \frac{\mathbf{u}}{\tau} + 3(\mathbf{u}\cdot\nabla_2\mathbf{u}) - 2\frac{u_\theta^2}{r}\mathbf{e}_r + 2C_L\mathbf{u}\times(\nabla\times\mathbf{u})$$
$$\downarrow \quad \downarrow \quad \downarrow \quad \downarrow$$
$$\underbrace{\frac{V_L}{\tau} \quad \frac{u'}{\tau}}_{\mathbf{e_z}} \qquad \underbrace{\frac{4u'u'}{e} \quad \frac{U_\theta^2}{R_1}}_{\mathbf{e_r}} \tag{11}$$

The order of magnitude of the various terms in (11) is readily evaluated by introducing the magnitude u' of the radial and vertical velocities within the Taylor vortices and that of the primary azimuthal velocity, U_θ. The factor of 4 in front of the fluid acceleration results from the fact that the secondary flow velocity varies from u' to zero within a distance of the order of $e/2$ and there are two contributions of equal magnitude in the velocity gradient, one in each direction of the $(\mathbf{e}_r-\mathbf{e}_z)$ plane. To characterize the bubbly flow configuration, it is then convenient to define two dimensionless parameters, C and H. Balancing the two contributions along the vertical direction $\mathbf{e}_z$ yields $C=u'/V_L$. Obviously, the z projection of (11) has a solution only if the magnitude of the downward velocity in the Taylor vortices is of the order of the limit rising speed of the bubbles at some point of the flow, a situation corresponding to the occurrence of closed bubble trajectories when buoyancy and drag balance each other in the vertical direction. In other words, entrapment is only possible if the global parameter C is at least of $O(1)$. This criterion is met in all entrapment processes of bubbles in vortical structures.[29] The second parameter, $H=4(u'/U_\theta)^2R_1/e$, compares the opposite trends of the inertial effects induced by the added mass, pressure gradient, and lift forces. The acceleration U_θ^2/R_1 based on the Couette flow pushes bubbles toward the inner cylinder, while $\mathbf{u}\cdot\nabla_2\mathbf{u}$ tends to capture them within the vortex cores.

Equilibrium positions of bubbles correspond to stable fixed points of the linearized equations (10) recasted within the form of a dynamical system. The corresponding stability analysis is performed following the method described in Ref. 29. The set of ordinary differential equations is similar to that encountered in the latter reference with the addition of the centripetal attraction $-U_\theta^2/r\mathbf{e}_r$. Solving numerically the projections of Eq. (11) in the $\mathbf{e}_r$ and $\mathbf{e}_z$ directions results in two curves whose intersections are the fixed points of the system. The stability of these fixed points is then analyzed by computing the eigenvalues of the Jacobian matrix of the dynamical system and examining the sign of their real part. Varying C and H independently and checking the stability of all fixed points allows us to obtain the complete phase diagram of the capture process.

An example of the location of the fixed points found for $H=128$ and $C=4.92$ is shown in Fig. 6(a). This corresponds to bubbles of 100 μm diameter released in pure water in the experimental device of Ref. 1, i.e., $R_1=4$ cm, $e=5$ mm. Four fixed points exist within the domain. Two of them, lying within the vortex cores, are stable ($r=8.43$,$z=1.41$ and $r=8.55$,$z=0.56$). The other two, clearly located outside the Taylor vortices, are unstable ($r=8.03$,$z=1.61$ and $r=8.96$,$z=0.74$). We checked the sensitivity of the location of the fixed points to the modeling of the lift force by changing the lift coefficient given by Eq. (8) into $C_L=1/2$. Only tiny modifications of the curve $f_r=0$ were observed, the most significant being located in the near-wall regions. This is a reassuring indication that the location of regions of bubble accumulation is almost insensitive to the lift force model (in contrast, the frontiers of the basin of attraction of a given fixed point and the bubble trajectories toward it may be more sensitive to this model). The trajectories of Fig. 6(b) show how bubbles are attracted by the stable fixed points. For this set of parameters, the flow domain is divided into two distinct basins of attraction. Bubbles released in the vicinity of the unstable fixed points move toward the stable fixed points of the corresponding attraction basin. As explained before, the location of the stable fixed point corresponds to the intersection of curves $f_r=0$ and $f_z=0$. Because $f_r=0$ is almost a horizontal straight line (from $r=8.25$ to 8.75), the radial location of the stable fixed point results from the solution of the equation $f_z=0$, i.e., from the force balance along the di-

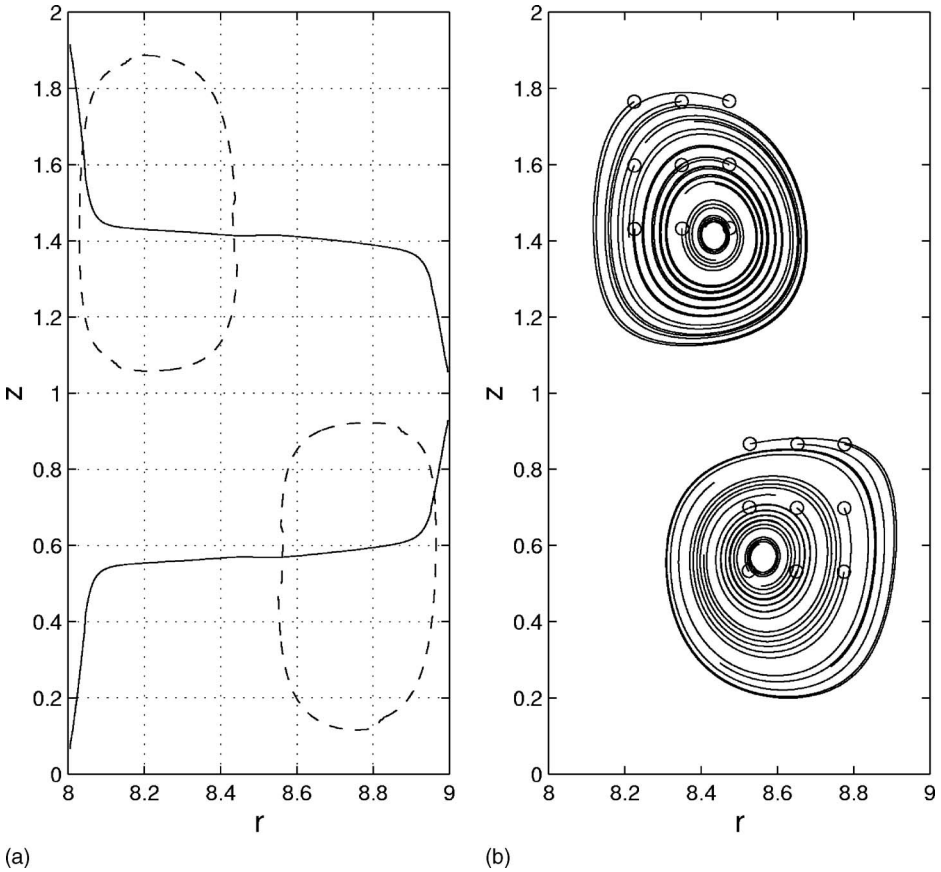

FIG. 6. Bubble evolution under flow conditions $H=128$, $C=4.92$. (a) Location of the fixed points (— $f_r=0$; --- $f_z=0$); (b) bubble trajectories (initial positions are marked with open circles).

rection of gravity. If we maintain H fixed and decrease C independently, the stable fixed points gradually move from the vortex cores toward a region of large downward flow velocity where the bubble slip velocity can be balanced by the negative vertical flow velocity. The complete phase diagram obtained by varying C and H is shown in Fig. 7. For low values of C, namely $C<2$ approximately, no fixed point exists and bubbles accumulate uniformly along the inner rotating cylinder, similarly to what we observed in the Couette flow regime. For higher C and $H>0.25$, approximately, the centripetal attraction toward the inner wall is counterbalanced by the vortex-induced pressure gradient and lift effects, so that bubbles are trapped within the Taylor vortices. The ratio of the strength of the pressure gradient force over that of the lift force along the radial direction is roughly (2:1). For large to moderate H, centripetal attraction toward the inner cylinder is counterbalanced by the $\mathbf{u}\cdot\nabla_2\mathbf{u}$ added-mass force in conjunction with the lift force. This corresponds to the situation depicted in Fig. 6. Decreasing H while C is maintained fixed corresponds to an enhancement of bubble attraction toward the inner wall while the strength of the Taylor vortices is frozen. When H is below a value of the order of 0.2 while C is still larger than 2, the attraction toward the vortex core is not able to counterbalance the centripetal migration and bubbles accumulate along the inner cylinder. However, this accumulation is nonuniform because bubbles cannot pass through the vortices since V_L remains smaller than u'. Hence, preferential accumulation occurs in the low-pressure zones of the inner wall. As may be seen in Fig. 2(b), these zones correspond to outflow regions ($r=8$ and $z=1$). The three basic scenarios we just described were observed in the experiments of Djéridi *et al.*,[2] indicating that the present dynamical system approach provides a correct view of the various mechanisms involved in the dispersion and accumulation of bubbles in the TVF regime. A difference between the computations and the experiments is that it is not possible to vary C and H independently in the latter because the amplitude of the secondary flow characterized by

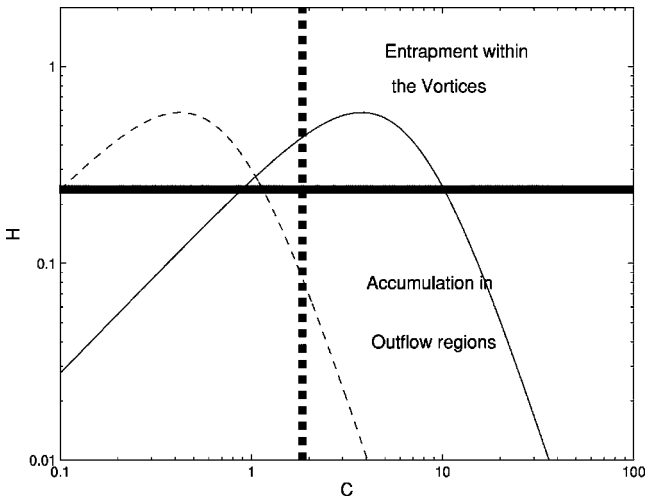

FIG. 7. (C,H) phase diagram of the final state of the bubbles. Curves refer to increasing rotation rates of the inner cylinder for a given Re_L. Solid line: $\mathrm{Re}_L=4.5$; dashed line: $\mathrm{Re}_L=41$.

u' is closely related to that of U_θ. However, we may use an indirect approach to explore how a given bubble evolves as the rotation rate is increased. For this, we start with the fact that the supercritical nature of the bifurcation leading to the TVF regime implies that, for rotation rates slightly beyond the threshold, the strength of the secondary velocity grows as[30]

$$u' = K\frac{\nu}{e}\left(\frac{\mathrm{Re}-\mathrm{Re}_o}{\mathrm{Re}_o}\right)^{1/2}, \tag{12}$$

where K is a constant that may be determined from Fig. 3. Using $\mathrm{Re}=U_\theta e/\nu$ and $\varepsilon=(\mathrm{Re}-\mathrm{Re}_o)/\mathrm{Re}_o$, we can express U_θ as $U_\theta=\mathrm{Re}_o\nu(1+\varepsilon)/e$. Therefore C and H can be recast in terms of Re_o, ε, and geometrical parameters as

$$C = K\frac{\nu}{V_L e}\varepsilon^{1/2}, \quad H = \frac{K^2}{\mathrm{Re}_o^2}\frac{4R_1}{e}\frac{\varepsilon}{(1+\varepsilon)^2}. \tag{13}$$

Experiments with fixed bubble characteristics and variable rotation rates of the inner cylinder in the TVF regime may then be parameterized as

$$H = \frac{K^2}{\mathrm{Re}_o^2}\frac{4R_1}{e}\frac{\left(\mathrm{Re}_L(C/K)\right)^2}{\left[1+\left(\mathrm{Re}_L(C/K)\right)^2\right]^2}, \tag{14}$$

where $\mathrm{Re}_L=V_L e/\nu$ is a bubble Reynolds number based on the slip velocity and the gap width. Both C and H are zero right at the threshold. The evolution of H with C is plotted in Fig. 7 for two different values of Re_L ($\mathrm{Re}_L=4.5$ corresponds to one set of the experiments in Refs. 1 and 2, while $\mathrm{Re}_L=41$ corresponds to the 100 μm bubbles of Fig. 6). H increases with C until it reaches its maximum $H_{\max}=(K/\mathrm{Re}_o)^2R_1/e$ for $C_{\max}=K/\mathrm{Re}_L$. When C further increases beyond $C_{\max}$, H decreases and tends asymptotically to zero for large C. For low values of C and H, bubbles are uniformly distributed along the inner wall. While the rotation rate, i.e., C, increases, H evolves following paths $H=f(C)$ such as those drawn in Fig. 7. As pointed out above, the transition to entrapment in Taylor vortices occurs when $C>2$ and $H>0.2$, approximately. Then, bubbles move toward the vortex cores where they accumulate around the stable fixed points, forming two distinct azimuthal rings. At higher values of C, i.e., faster rotation rates, the centripetal acceleration toward the wall overcomes the attraction by the vortices. Hence the stable fixed points disappear and bubbles collect at the inner wall in the regions of outflow. This is why only a single ring of bubbles is observed in our computational domain under such conditions. Such a transition from two to one single bubble ring per wavelength of the TVF has been observed experimentally (see Fig. 8). Note that in experiments, it is not possible to cover the whole range of H as we did here because the second bifurcation leading to the wavy vortex flow regime occurs for some finite value of H. Numerically, we are of course able to make H as large as we wish by constraining the flow to remain independent of the azimuthal position, thus preventing the transition to the WVF.

The experiments by Djéridi *et al.*[1] reveal a gradual evolution of the axial distance between the two bubble rings followed by a sharp transition toward the single bubble ring pattern. It is of interest to see how the numerical predictions compare with these observations. The evolution of the axial distance between the stable fixed points with H for one of the parameter sets investigated in Ref. 1 (1 mm diameter bubbles with $V_L=2.72\times10^{-2}$ m/s in a glycerol/water solution with $\nu=3.0\times10^{-5}$ m^2/s, corresponding to $\mathrm{Re}_L=4.5$) is plotted in Fig. 9. When the rotation rate (i.e., C) increases and H is beyond a critical value (here $H=0.25$), the distance D between the two rings decreases continuously, starting from the value $D=0.4e$. This decrease is small until the parameter H reaches its maximum $H=0.47$. Then, for larger C, H decreases and the distance between the two rings decreases much more rapidly until only a single ring remains when bubbles accumulate in the region of outflow for $H<0.28$. In the experiments as well as in the computations, the transition from the two-ring configuration to the single-ring one sets in for a value of H that only weakly depends on the bubble characteristics (V_L or Re_L). Among other things, this means that with a polydisperse distribution of bubbles, the transition should be observed almost simultaneously for all bubble diameters. When transformed back in dimensional form, the numerical prediction indicates that the transition

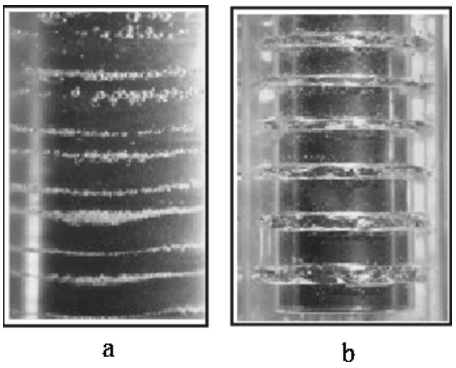

FIG. 8. Experimental visualizations of the organized gaseous phase in the gap for different reduced Reynolds numbers [from Djéridi *et al.* (Ref. 2)]. (a) $\mathrm{Re}/\mathrm{Re}_{c1}=4.5$: two bubble strings per axial wavelength. (b) $\mathrm{Re}/\mathrm{Re}_{c1}=11$, one single bubble string per axial wavelength.

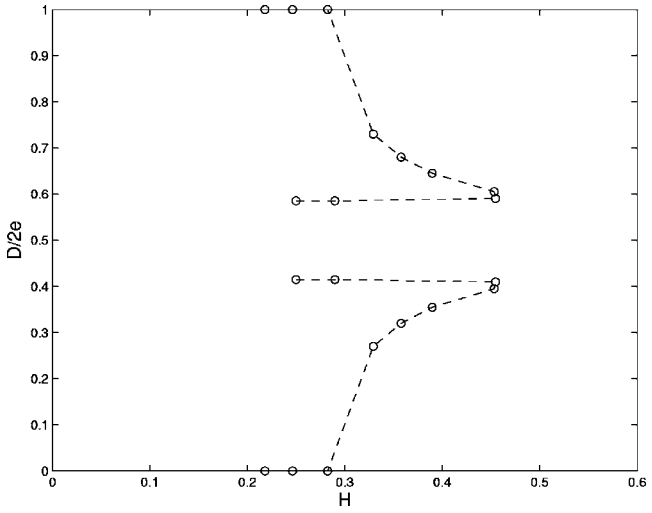

FIG. 9. Evolution of the distances between two consecutive bubble rings ($\mathrm{Re}_L=4.5$).

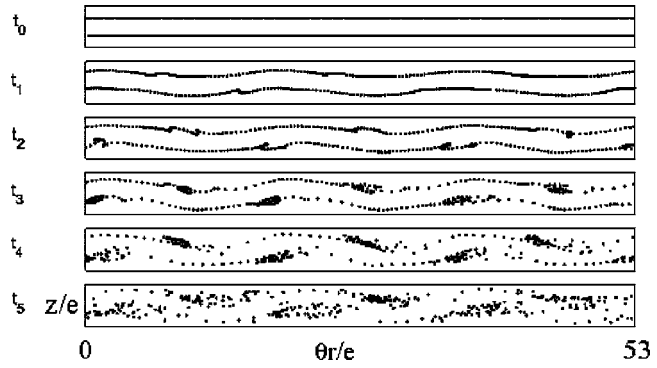

FIG. 10. Snapshots of bubble positions during the transient evolution from TVF to WVF (t_o: pure TVF; t_5: the wave amplitude of the WVF has saturated). The visualization plane $(\mathbf{e}_\theta, \mathbf{e}_z)$ is located midway between the two cylinders ($r=8.5$).

occurs at a critical rotation rate about 160 rad/s. This prediction is in good agreement with the value of 1800 rpm (i.e., 188.5 rad/s) determined by Djéridi *et al.*[1] This agreement suggests that our model approach does not only provide the basic features of bubble dispersion in TVF but also delivers predictions in quantitative agreement with observations.

B. Bubble dispersion in the wavy vortex flow regime

The Couette-Taylor flow undergoes a second bifurcation when $\mathrm{Ta}=\mathrm{Ta}_1$ (or $\mathrm{Re}=\mathrm{Re}_1$). Taylor vortices tend to undulate and an azimuthal wave grows up. When this transition occurs for values of H higher than the critical value corresponding to the migration toward outflow regions, bubbles remain trapped in the vortices. As shown in Fig. 10, when the amplitude of the azimuthal wave grows, bubble positions follow closely the oscillations of the vortices. The azimuthal location of the bubbles becomes gradually nonuniform. Bubbles preferentially accumulate at the crests and troughs of the wavy vortex cores. In this simulation, the wavy oscillation is characterized by a dimensionless azimuthal wave number $k_\theta=3$, where the reference length is $\pi(R_1+R_2)$. $k_\theta=3$ corresponds to three wavelengths along the cylinder perimeter. A similar nonuniform distribution was also observed in the aforementioned experiments.[1,2] However, bubble coalescence quickly occurred because of the local increase of the bubble volume fraction in the accumulation zones: instead of small bubbles collected at crests and troughs of wavy vortices, large bubbles were observed. This increase in the bubble size cannot be captured in our computations since they do not include any coalescence model. Figure 11 indicates that preferential bubble accumulation is closely related to the local minima of the relative pressure. The corresponding flow pattern has a dimensionless azimuthal wave number $k_\theta=2$ ($\mathrm{Re}=167=1.33\mathrm{Re}_o$; $\varepsilon=0.336$) and a dimensionless phase velocity $\omega/k_\theta\Omega=0.44$ (in agreement with Jones[31]). The azimuthal component of the slip velocity is negligible and bubbles move with the local fluid velocity. We checked that the local fluid velocity at $r/e=8.5$ is equal to the phase velocity of the wavy modulation of the vortices. Therefore, bubbles are able to move with the local minima of pressure while remaining trapped close to the crests and troughs of the vortices. Examining the evolution of bubble locations with r indicates that bubble accumulation takes place essentially in the middle of the gap. If the Reynolds number based on the inner cylinder rotation is increased further, bubbles are no longer trapped in the vortices. This change occurs because the coherence of the wavy vortices decreases gradually since the axial flow that connects two successive counter-rotating vortices grows while ε increases (Fig. 12). This feature was clearly emphasized experimentally by Akonur and Lueptow,[32] who observed these axial flows in the WVF regime using particle image velocimetry. Such streams turn out to be strong enough to drive bubbles outside the vortices and to disperse them more evenly than in the TVF regime. At higher Reynolds number, the flow becomes chaotic and vortex cores disappear. However, coherent vortices may reappear when the rotation rate is increased further, suggesting that bubble dispersion may again be closely related to the presence of strong coherent structures.[3]

IV. CONCLUSION

We numerically investigated the dispersion of bubbles within the first three distinct flow regimes encountered in the Couette-Taylor configuration and found that this dispersion is dramatically affected by the successive bifurcations of the flow. Our simulations are based on an individual Lagrangian tracking of bubbles coupled with a direct numerical simulation of the carrying fluid flow. The trajectory computation is supplemented by a theoretical determination of accumulation regions, which shows that bubbles tend to accumulate either around the stable fixed points of the two-phase flow when they exist, or in the low-pressure regions located near the inner cylinder, which correspond to outflow regions. Numerical results reveal a very good agreement with experimental findings.[1,2]

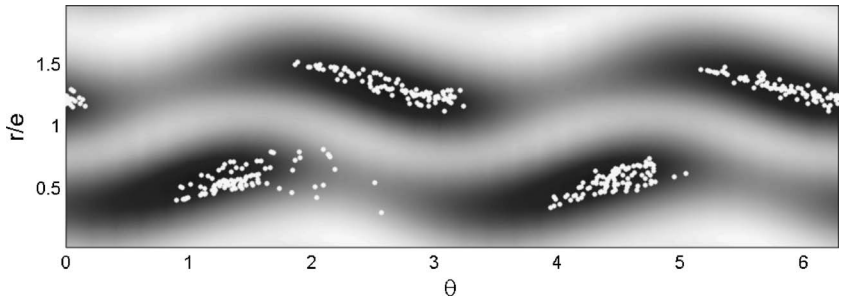

FIG. 11. Bubble positions (white dots) and local pressure contours in the middle of the gap ($r=8.5$). Dark areas correspond to low pressures.

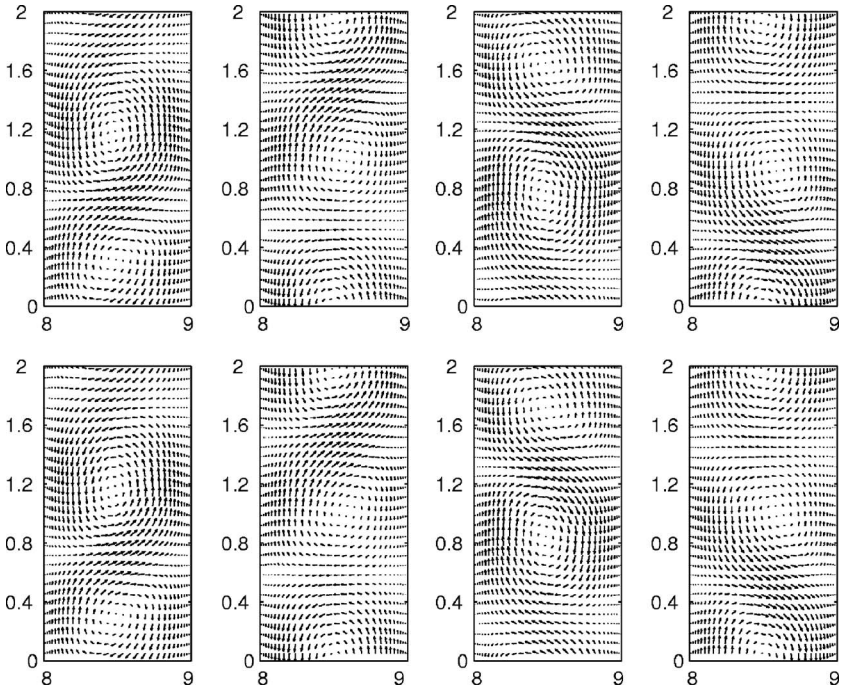

FIG. 12. Consecutive velocity fields along the azimuthal wavy oscillation (from top left to bottom right) for $k_\theta = 2$ and Re=167.

The computational results help better understand the experimental observations. At low rotation rate, the purely azimuthal Couette flow induces a migration of the bubbles toward the inner cylinder. A uniform distribution of rising bubbles develops along the vertical inner cylinder. When the first bifurcation occurs, a secondary flow made of counter-rotating vortices sets in. The strength of these vortices increases with the flow Reynolds number and bubbles are eventually trapped within the cores of these steady coherent vortices. In this case, the centripetal attraction toward the vortex cores overcomes the migration toward the inner wall. Bubbles are accumulating close to the vortex centers on the side where the downward fluid velocity balances the buoyancy-induced slip velocity. This accumulation results from the occurrence of spiralling pathlines in any vertical cross section of the gap, which themselves result from (a) the existence of downward fluid velocities of the order of the bubble rise velocity (a situation that would lead to closed pathlines in the absence of inertia effects) and (b) the centripetal attraction induced by inertial effects toward the vortex cores. Accumulation positions obviously correspond to the stable fixed points of the linearized dynamical system associated with the bubble paths. Two circular rings along which bubbles accumulate are observed along the azimuthal direction. Depending on the bubble characteristics, two distinct behaviors may occur when the rotation rate of the inner cylinder is further increased. First, the attraction toward the inner wall may increase faster than the strength of the Taylor vortices, and stable fixed points may then disappear. In this case, bubbles accumulate in the outflow regions located between two counter-rotating vortices on the inner wall. This bifurcation of the bubble dispersion pattern has been observed experimentally. It corresponds to a single bubble ring per wavelength of the flow. The numerical transition criterion $H \approx 0.2$ compares favorably with the experiments and is only weakly dependent on the bubble size. On the other hand, if bubbles stay trapped in the Taylor vortices when the second instability of the flow occurs, a nonuniform accumulation of bubbles is observed in the WVF regime. The two bubble rings gradually disappear while the wavy modulation of the vortices develops. Bubbles accumulate at the crests and troughs of the undulating vortices, which correspond to local minima of the pressure field. Finally, bubbles escape from the vortices when the axial streams connecting two successive counter-rotating vortices reach a sufficient magnitude. Vortex cores rapidly disappear in the WVF regime but reappear when the Reynolds number increases further, indicating that bubble entrapment may occur in other flow regimes.

Although our numerical model involves several assumptions, the present study indicates that it provides a powerful tool to investigate and understand the basic features of bubble dispersion in a centrifugal flow. We only performed one-way coupling simulations in which the interphase momentum transfer induced on the fluid by the presence of bubbles was neglected. In a dilute bubbly flow, such an assumption is uniformly valid if bubbles are evenly dispersed. However, we showed that bubbles accumulate in particular regions of the flow. The local dynamics of the flow may then be modified by two-way coupling effects, and direct interactions between the bubbles may lead to complex phenomena such as coalescence. Moreover, the presence of a significant amount (i.e., some percents) of bubbles may modify the flow structure and the thresholds of the successive flow bifurcations. Some preliminary experimental results of these interactions for bubbly flows were presented by Djéridi *et al.*[1] and Mehel *et al.*[10] Depending on the location of bubble accumulation, they observed that wall-shear stress and axial transfer can be significantly modified. Two-way coupling simulations may be desirable to investigate the couplings between bubble

dispersion and flow distortions due to the dispersed phase. In particular, they may help to elucidate the flow modifications induced by the transition in the bubble dispersion as well as the changes that the flow distortion induces in the bubble dispersion. When the flow is turbulent, bubble injection dramatically modifies its response and eventually provokes a reduction of the torque it exerts on the rotating cylinder.[33] Ali *et al.*[34] carried out a linear stability analysis of a cylindrical two-phase Couette flow of a dilute suspension of rigid spherical particles. They found that the critical Taylor number at which Taylor vortices first appear decreases as the particle concentration increases. Moreover, they noticed that increasing the ratio of particle-to-fluid density above 1 decreases the stability of the overall flow pattern, whereas the axial wave number is left unchanged by the two-phase nature of the flow. Exploring such effects of two-way coupling will be the purpose of the next step of our work.

[1] H. Djéridi, C. Gabillet, and J. Y. Billard, "Two-phase Couette-Taylor flow: Arrangement of the dispersed phase and effects on the flow structures," Phys. Fluids **16**, 128 (2004).
[2] H. Djéridi, J. F. Favé, J. Y. Billard, and D. H. Fruman, "Bubble capture and migration in Couette-Taylor flow," Exp. Fluids **26**, 233 (1999).
[3] K. Atkhen, J. Fontaine, and J. E. Wesfreid, "Highly turbulent Couette-Taylor bubbly flow patterns," J. Fluid Mech. **422**, 55 (2000).
[4] M. Rudman, "Mixing and particle dispersion in the wavy vortex regime of Taylor-Couette flow," AIChE J. **44**, 1015 (1998).
[5] M. Rudolph, T. Shinbrot, and R. M. Lueptow, "A model of mixing and transport in wavy Taylor-Couette flow," Physica D **121**, 163 (1998).
[6] Y. Shiomi, H. Kutsuna, K. Akagawa, and M. Ozawa, "Two-phase flow in an annulus with a rotating inner cylinder (flow pattern in bubbly flow region)," Nucl. Eng. Des. **141**, 27 (1993).
[7] K. J. Sene, J. C. R. Hunt, and N. H. Thomas, "The role of coherent structures in bubble transport by turbulent shear flow," J. Fluid Mech. **259**, 219 (1994).
[8] R. E. G. Poorte and A. Biesheuvel, "Experiments on the motion of gas bubbles in turbulence generated by an active grid," J. Fluid Mech. **461**, 127 (2002).
[9] G. Sridhar and J. Katz, "Effect of entrained bubbles on the structure of vortex rings," J. Fluid Mech. **397**, 171 (1999).
[10] A. Mehel, C. Gabillet, and H. Djeridi, "Bubble effect on the structures of weakly turbulent Couette-Taylor flow," J. Fluids Eng. **128**, 819 (2006).
[11] I. Calmet and J. Magnaudet, "Statistical structure of high-Reynolds-number turbulence close to the free surface of an open-channel flow," J. Fluid Mech. **474**, 355 (2003).
[12] D. Legendre and J. Magnaudet, "The lift force on a spherical bubble in a viscous linear shear flow," J. Fluid Mech. **368**, 81 (1998).
[13] P. S. Marcus, "Simulation of Taylor-Couette flow. Part 1. Numerical methods and comparison with experiment," J. Fluid Mech. **146**, 45 (1984).
[14] S. Chandrasekhar, *Hydrodynamic and Hydromagnetic Stability* (Oxford University Press, Oxford, UK, 1961).
[15] R. C. Di Prima and H. L. Swinney, *Hydrodynamic Instabilities and the Transition to Turbulence* (Springer, New York, 1981).
[16] C. D. Andereck, S. S. Liu, and H. L. Swinney, "Flow regimes in a circular Couette system with independently rotating cylinders," J. Fluid Mech. **164**, 155 (1986).
[17] D. Coles, "Transition in circular Couette flow," J. Fluid Mech. **21**, 385 (1965).
[18] P. R. Fenstermacher, H. L. Swinney, and J. P. Gollub, "Dynamical instabilities and the transition to chaotic Taylor-Vortex flow," J. Fluid Mech. **94**, 103 (1979).
[19] R. Gatignol, "The Fàxen formulae for a rigid particle in unsteady non-uniform Stokes flow," J. Mec. Theor. Appl. **1**, 143 (1983).
[20] M. R. Maxey and J. J. Riley, "Equation of motion for a small rigid sphere in a non-uniform flow," Phys. Fluids **26**, 883 (1983).
[21] J. Magnaudet and I. Eames, "The motion of high-Reynolds-number bubbles in inhomogeneous flows," Annu. Rev. Fluid Mech. **32**, 659 (2000).
[22] M. Rivero, J. Magnaudet, and J. Fabre, "Quelques résultats nouveaux concernant les forces exercées sur une inclusion sphérique par un écoulement accéléré," C. R. Acad. Sci., Ser. II: Mec., Phys., Chim., Sci. Terre Univers **312**, 1499 (1991).
[23] J. Magnaudet, M. Rivero, and J. Fabre, "Accelerated flows past a rigid sphere or a spherical bubble. Part I: Steady straining flow," J. Fluid Mech. **284**, 97 (1995).
[24] D. Legendre and J. Magnaudet, "The lift force on a spherical bubble in a viscous linear shear flow," J. Fluid Mech. **368**, 81 (1998).
[25] J. Magnaudet, "Inertial effects of a spherical bubble, drop or particle moving near a wall in a time-dependent linear flow," J. Fluid Mech. **485**, 115 (2003).
[26] J. Magnaudet and D. Legendre, "Some aspects of the lift force on a spherical bubble," Appl. Sci. Res. **58**, 441 (1998).
[27] E. A. van Nierop, S. Luther, J. J. Bluemink, J. Magnaudet, A. Prosperetti, and D. Lohse, "Drag and lift forces in a rotating flow," J. Fluid Mech. **571**, 439 (2007).
[28] B. D. Marsch and M. R. Maxey, "On the distribution and separation of crystals in convecting magma," J. Volcanol. Geotherm. Res. **24**, 95 (1985).
[29] E. Climent and J. Magnaudet, "Dynamics of a two-dimensional upflowing mixing layer seeded with bubbles: Bubble dispersion and effect of two-way coupling," Phys. Fluids **18**, 103304 (2006).
[30] J. P. Gollub and M. H. Freilich, "Optical heterodyne test of perturbation expansions for the Taylor instability," Phys. Fluids **19**, 618 (1976).
[31] C. A. Jones, "Nonlinear Taylor vortices and their stability," J. Fluid Mech. **102**, 249 (1981).
[32] A. Akonur and R. M. Lueptow, "Three-dimensional velocity field for wavy Taylor-Couette flow," Phys. Fluids **15**, 947 (2003).
[33] T. H. Van den Berg, S. Luther, D. P. Lathrop, and D. Lohse, "Drag reduction in bubbly Taylor-Couette turbulence," Phys. Rev. Lett. **94**, 044501 (2005).
[34] M. E. Ali, D. Mitra, J. A. Schwille, and R. M. Lueptow, "Hydrodynamic stability of a suspension in cylindrical Couette flow," Phys. Fluids **14**, 1236 (2002).
[35] R. J. Donnelly and N. J. Simon, "An empirical torque relation for supercritical flow between rotating cylinders," J. Fluid Mech. **7**, 401 (1960).
[36] A. Davey, "The growth of Taylor vortices in flow between rotating cylinders," J. Fluid Mech. **14**, 336 (1962).